[CANCER RESEARCH 63, 6689–6696, October 15, 2003]

Fluorescence Imaging of Multiple Myeloma Cells in a Clinically Relevant SCID/NOD *in Vivo* Model: Biologic and Clinical Implications[1]

Constantine S. Mitsiades,[2, 3] Nicholas S. Mitsiades,[3] Ron T. Bronson, Dharminder Chauhan, Nikhil Munshi, Steven P. Treon, Christopher A. Maxwell, Linda Pilarski, Teru Hideshima, Robert M. Hoffman, and Kenneth C. Anderson[2]

Jerome Lipper Multiple Myeloma Center, Department of Medical Oncology, Dana-Farber Cancer Institute, Boston, Massachusetts 02115 [C. S. M., N. S. M., D. C., N. M., S. P. T., T. H., K. C. A.]; Departments of Medicine [C. S. M., N. S. M., D. C., N. M., S. P. T., T. H., K. C. A.] and Pathology [R. T. B.], Harvard Medical School, Boston, Massachusetts 02115; Cross Cancer Institute, University of Alberta, Edmonton, Alberta, T6G 1Z2 Canada [C. A. M., L. P.]; and Department of Surgery, University of California at San Diego, San Diego, California 92111 [R. M. H.]; and AntiCancer, Inc., San Diego, California 92111 [R. M. H.]

ABSTRACT

The *in vivo* preclinical testing of investigational therapies for multiple myeloma (MM) is hampered by the fact that models generated to recapitulate the development of diffuse skeletal lesions after i.v. injections of tumor cells do not allow for ready detection of the exact site(s) of lesions or for comprehensive monitoring of their progression. We therefore developed an *in vivo* MM model in severe combined immunodeficient/nonobese diabetic mice in which diffuse MM lesions developed after tail vein i.v. injection of human RPMI-8226/S MM cells stably transfected with a construct for green fluorescent protein (GFP). Using whole-body real-time fluorescence imaging to detect autofluorescent GFP^+ MM cells (and confirming the sensitivity and specificity of these findings both histologically and by flow cytometric detection of GFP^+ cells), we serially monitored, in a cohort of 75 mice, the development and progression of MM tumors. Their anatomical distribution and pathophysiological manifestations were consistent with the clinical course of MM in human patients, *i.e.*, hallmarked by major involvement of the axial skeleton (*e.g.*, spine, skull, and pelvis) and frequent development of paralysis secondary to spinal lesions without significant tumor spread to lungs, liver, spleen, or kidney. This model both recapitulates the diffuse bone disease of human MM and allows for serial whole-body visualization of its spatiotemporal progression. It therefore provides a valuable *in vivo* system to elucidate the molecular mechanisms underlying the marked osteotropism of MM, particularly for the axial skeleton, and for assessment of *in vivo* activity of novel anti-MM therapeutics.

INTRODUCTION

The development of *in vivo* animal models that recapitulate the natural history of human cancers and their clinical response to therapy constitutes a major prerequisite for rapid bench-to-bedside translation of investigational anticancer therapies. However, most conventional *in vivo* models for preclinical evaluation of anticancer drugs have, in general, involved s.c. implantation of tumor cells in immunodeficient mice. Unfortunately, such models cannot accurately simulate the *in vivo* behavior and drug-sensitivity patterns of human neoplasias, especially hematological malignancies such as MM.[4] s.c. xenograft models failed not only to reflect the systemic nature of diffuse lesions of MM and other hematological malignancies but also place tumor cells in the cutaneous microenvironment, which is radically different from the BM milieu, where MM cells are preferentially homing and which promotes their proliferation, survival, and resistance to therapy (*e.g.*, dexamethasone) via adhesion of MM cells to BMSCs and ECM proteins and the local production of cytokines (1, 2). This limitation of s.c. xenograft models is critical because the interactions between tumor cells and their local microenvironment cannot only explain, at least in part, the tropism of tumors for certain metastatic sites but may also influence their responsiveness to therapy (1–3). Although the systemic nature of hematological malignancies may be recapitulated by *in vivo* models of i.v. injections of tumor cells such as in SCID/NOD models of MM (4), these models do not readily allow for sensitive, real-time detection of the exact anatomical site(s) of development of lesions or for comprehensive monitoring of their progression.

To address these limitations of conventional *in vivo* models for hematological malignancies, we developed an *in vivo* model of MM where MM cells stably transfected with construct for the GFP of the jellyfish *Aequorea Victoria* are injected i.v. in SCID/NOD mice: the subsequent development of diffuse MM lesions can be monitored by whole-body fluorescence imaging, which detects the fluorescence emitted by the GFP^+ MM cells when illuminated with near-infrared light. Because of the marked visual contrast generated between fluorescent GFP^+ MM cells and nonfluorescent GFP^- normal tissues of the host, we were able to visualize noninvasively and monitor serially, the anatomical distribution of MM lesions in the intact mouse, including s.c. tissues, bone, and BM, as well as visceral sites of tumor infiltration.

This first GFP-based *in vivo* model of a hematological malignancy represents a new avenue of research distinct from previous applications of fluorescence imaging in solid tumor models (5–13). Herein, this GFP model recapitulates the diffuse bone disease of MM, and importantly, the anatomical distribution of GFP^+ lesions, confirmed by flow cytometry and extensive histopathological analyses, is consistent with the distribution of tumors in MM patients and, in particular, their preferential development in sites of the axial skeleton. Therefore, this study not only provides a clinically relevant *in vivo* model for more accurate preclinical evaluations of investigational therapies against MM but also generates a reproducible framework to characterize the interactions of MM cells with the BM milieu *in vivo*, with particular emphasis on the preferential targeting by MM cells of distinct areas of the skeleton. Because the BM microenvironment is now emerging as a key aspect of the pathophysiology of other hematological malignancies and not just MM, our study constitutes a framework for development of similar models for those diseases as well.

MATERIALS AND METHODS

Stable Transfection of GFP Constructs in MM Cells. The human MM cell line RPMI 8226 was cultured in RPMI 1640 supplemented with 10% fetal

Received 3/16/03; revised 6/2/03; accepted 7/1/03.

The costs of publication of this article were defrayed in part by the payment of page charges. This article must therefore be hereby marked *advertisement* in accordance with 18 U.S.C. Section 1734 solely to indicate this fact.

[1] Supported by the Multiple Myeloma Research Foundation (to C. S. M., N. M.), Lauri Strauss Leukemia Foundation (to C. S. M., N. M.), International Waldenstrom's Macroglobulinemia Foundation (to C. S. M.), National Institutes of Health Grants RO-1 50947 and PO-1 78378, and Doris Duke Distinguished Clinical Research Scientist Award (to K. C. A.). C. S. M. is a Special Fellow of the Leukemia and Lymphoma Society.

[2] To whom requests for reprints should be addressed, at Jerome Lipper Multiple Myeloma Center, Department of Medical Oncology, Dana-Farber Cancer Institute, Harvard Medical School, 44 Binney Street, Boston MA 02115. Phone: (617) 632-1962; Fax: (617) 812-7701; E-mail: Constantine_Mitsiades@dfci.harvard.edu and Kenneth_Anderson@dfci.harvard.edu.

[3] Both authors contributed equally to this work.

[4] The abbreviations used are: MM, multiple myeloma; BM, bone marrow; BMSC, BM stromal cell; ECM, extracellular matrix; SCID/NOD, severe combined immunodeficient/nonobese diabetic; GFP, green fluorescent protein; MTT, 3-(4,5-dimethylthiazol-2-yl)-2,5-diphenyltetrazolium bromide; CI, confidence interval.

bovine serum, penicillin, streptomycin, and L-glutamine. Near-confluent RPMI-8226/S cells were incubated with a precipitated mixture of Lipofectamine 2000 (Life Technologies, Inc., Gaithersburg, MD) and saturating amounts of the GFP-expressing pLNCX$_2$-GFP plasmid for 6 h, and fresh medium was then added. Forty-eight h after transfection, RPMI-8226/S cells were subcultured at a ratio of 1:15 in selection medium containing 500 μg/ml G418 (Life Technologies, Inc.) to isolate cells with stably integrated GFP plasmids.

MTT Colorimetric Survival Assay. RPMI-8226/S cells transfected with GFP or control (neo) vector were incubated with 250 ng/ml doxorubicin (Sigma Chemical Co., St. Louis, MO) for 48 h, and cell survival was assessed by MTT colorimetric survival assay (14).

SCID/NOD Mice and MM Cell Injection. A cohort of 85 male (6–8-week old) immunodeficient SCID/NOD mice were obtained from The Jackson Laboratory (Bar Harbor, ME) and were housed and monitored in the Animal Research Facility of the Dana-Farber Cancer Institute. All experimental procedures and protocols had been approved by the Institutional Animal Care and Use Committee. Mice were γ-irradiated (300 rads) using a ^{137}Cs γ-irradiator source. After 24 h, 75 mice received tail vein injections of 5×10^6 RPMI-8226/S-GFP$^+$ cells suspended in a total volume of 100 μl PBS/mouse, whereas a control cohort of 10 mice received equal volume of PBS i.v. injections. Mice were monitored daily for changes in their body weight, signs of infection, and paralysis and thrice weekly by fluorescence imaging. In accordance with institutional guidelines, mice were sacrificed by CO_2 inhalation in the event of paralysis or major compromise in their quality of life.

Whole-Body Real-Time Fluorescence Imaging. The development of fluorescent MM lesions in the skeleton and extraskeletal sites was periodically monitored by whole-body fluorescence imaging using the LT-9500 fluorescent light box (Lightools Research, Encinitas, CA). Fluorescence excitation of GFP tumors was produced through a 440 $\pm$ 20-nm interference filter (excitation filter) using slit fiber optics for animal illumination. Fluorescence was observed through a 520-nm long pass filter (viewing filter). Fluorescence imaging results were digitally captured on a FujiFilm FinePix 6800Z digital camera (FujiFilm USA, Edison, NJ) and analyzed with Adobe PhotoShop 7.0 and Image Pro Plus v.4.0 software (Media Cybernetics, Silver Spring, MD). Before fluorescence imaging, cutaneous hair of the mice was removed with Nair (Carter-Wallace, New York, NY).

Fluorescence Imaging-Guided Necropsy. During necropsy of sacrificed mice, fluorescence imaging-guided macroscopic inspection of internals organs was performed after generation of skin flaps (to evaluate whether the autofluorescence of GFP$^+$ tumors is attenuated by the skin), as well as during the preparation of the spine, lung, liver, and spleen after the dissection of each specimen but before additional processing for histopathological analysis. Samples from the spine, skull, pelvis, extremities, thoracic cage, s.c. tissue, or any other organ that contained fluorescing lesions (as well as control samples obtained from sites adjacent to fluorescent lesions or from unaffected contralateral sites) were processed for conventional histopathological examination.

Flow-Cytometric Analysis of s.c. Plasmacytomas and BM Aspirates. s.c. plasmacytomas from GFP$^+$-injected mice (or s.c. tissue from control mice) were removed during necropsy and kept in PBS until processing for preparation of single-cell suspensions. BM aspirates from both femoral bones were obtained from all GFP$^+$-injected and control mice by flushing PBS into the marrow cavity of femoral bones and were processed for RBC lysis. All samples were then analyzed with flow cytometry, using RPMI-8226/S-GFP$^+$ cells growing in monolayer cultures as positive controls and neo (vector)-transfected RPMI-8226/S cells as negative controls. Counterstaining of GFP$^+$ MM cells was performed with phycoerythrin-conjugated antihuman CD38 monoclonal antibody (Beckman Coulter, Miami, FL). All flow cytometric analysis (single color-flow cytometry for assessment of GFP$^+$ and dual color cytometry for GFP$^+$ status and CD38$^+$ expression) was performed according to previously described protocols (14–16) and analyzed on an Epics-XL-MCL flow cytometer (Beckman Coulter).

Statistical Analysis. The overall survival of mice was defined as the time between i.v. injection of tumor cells and sacrifice or death. Kaplan-Meier survival analysis was performed as described previously (17). To confirm that differences in frequency of development of tumor lesions in individual organs are statistically significant, we calculated the 95% CI of each frequency as described previously (18). A difference in frequencies of tumor involvement for two organs or tissues was considered significant ($P < 0.05$) if the 95% CI of two compared frequencies of tumor involvement had no overlap (18).

Fluorescent Imaging Cross-Sections. After acquisition of external fluorescent images, 15 of the 80 mice of our cohort were kept at -80°C for 12–24 h, then sliced in cross-section at ~10-mm thickness using disposable microtome blades (Model 818; Leica) The sections were observed both under fluorescence microscopy or fluorescence light box imaging, simulating the acquisition of tomographic images to confirm the tumor localization determined by external visualization using whole-body fluorescence imaging.

Histolopathological Analysis. Immediately after fluorescence imaging-guided necropsy, specimens from tissues with fluorescent lesions, as well as representative samples of nonfluorescent areas of several organs (lungs, liver, spleen, and so on) were fixed in 10% buffered formalin; skeletal tissues were decalcified with 14% EDTA and embedded in paraffin by previously described standard techniques (19, 20). Soft tissues were fixed in 10% buffered formalin and embedded in paraffin without prior decalcification. Nonconsecutive sections were cut longitudinally using a standard microtome through the sagittal plane of the lumbar vertebrae and through blocks of liver, spleen, lung, kidney, intestines, s.c. tissue, and other specimens in each animal. The sections were then placed on poly-L-lysine-coated glass slides and stained with H&E (19, 20).

Whole-Body Radiographic Analysis. After sacrifice, whole body radiographs were obtained with a Faxitron radiographic inspection unit (Field Emission Corporation, Inc., McMinnville, OR) as described previously (21). After tissue dissection, removal of the skin, and fixation in 10% buffered formalin, similar radiographs were also taken of the limbs, spine, and calvaria.

RESULTS

Isolation of Stable, High Level-Expression GFP Transfectants of RPMI 8226 Cells. RPMI-8226/S cells transfected with GFP or control (neo) vector were selected in multiple steps for growth in levels of geneticin (G418) up to 500 μg/ml, as well as for high expression of GFP, which was confirmed by flow cytometric analysis of RPMI-8226/S-GFP$^+$ cells *versus* parental RPMI-8226/S cells (Fig. 1*A*). GFP$^+$ cells retained bright GFP fluorescence after numerous passages in the absence of selective agents, whereas their responsiveness to conventional anti-MM drugs, *e.g.*, doxorubicin, did not significantly differ from control RPMI-8266/S cells (Fig. 1*B*).

Whole-Body Fluorescence Imaging of GFP$^+$ MM Lesions. Serial whole-body fluorescence imaging of SCID/NOD mice allowed external visualization of GFP$^+$ tumors growing s.c. and/or internally. Whole-body fluorescence imaging of SCID/NOD mice 3–4 weeks after i.v. injection of RPMI-8226/S-GFP$^+$ cells demonstrated development of GFP$^+$ MM lesions in multiple skeletal, as well as extraskeletal (*e.g.*, s.c.) sites (Fig. 2). Table 1 summarizes the anatomical distribution (with 95% CIs of site-specific frequencies) of MM lesions in a cohort of 75 SCID/NOD mice that received injected with RPMI-8226/S-GFP$^+$ cells. The overwhelming majority of mice (74 of 75 mice, 98.7%, 95% CI: 92.9–100) developed skeletal lesions. Specifically, 72 of 75 mice (96.0%, 95% CI: 88.9–99.7) developed lesions in their spine, primarily lumbar (57 of 75 mice, 76.0% of mice, 95% CI: 65.2–84.2), and thoracic (39 of 75 mice, 52.0%, 95% CI: 40.8–63.0) vertebrae, whereas in a great majority of cases (64 of 75 mice, 85.3%), MM lesions were detected in the skull. Extraskeletal lesions were also formed, including s.c. plasmacytomas in 50 of 75 mice (66.7%, 95% CI: 55.4–76.3), and plasmacytomas in soft tissues of the posterior cervical area in 49 of 75 mice (65.3%, 95% CI: 54.0–75.1). Interestingly, however, visceral MM lesions in lung, liver, spleen, or kidney developed only rarely (<5% of mice). The development of spinal lesions was associated with hind limb paralysis (78.8% of mice), after a median of 29 days (range, 22–43 days), prompting sacrifice of mice per protocol (Fig. 3).

GFP$^+$ MM cells in this model home primarily to bone directly adjacent to skin, facilitating external imaging of these lesions. To

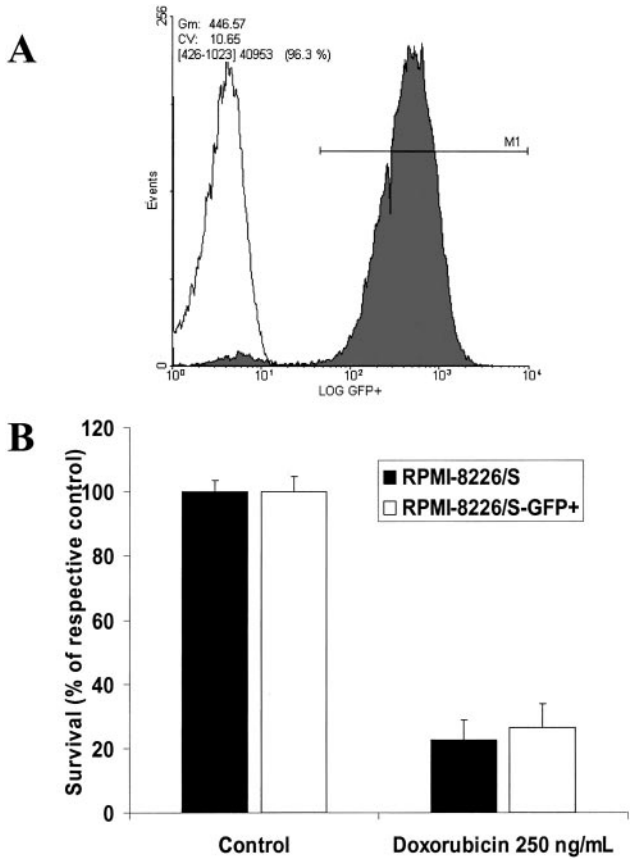

Fig. 1. *A*, flow cytometric analysis (FL1 channel) indicates a ~2-log difference in mean fluorescence intensity of RPMI-8226/S-GFP$^+$ cells (■) *versus* control RPMI-8226/S transfected with empty (neo) vector (□). *B*, after a 48-h incubation with doxorubicin (250 ng/ml), MTT colorimetric assay indicates that there is no difference in the survival of RPMI-8226/S control cells *versus* RPMI-8226/S-GFP$^+$ cells.

address the possibility that internal organs may harbor small visceral fluorescent lesions that could not be detected externally because of light scattering in intervening tissue, we performed postsacrifice opening of skin-flaps in the light path to reduce signal attenuation and increase detection sensitivity (5). As in previous studies, the observable depth of tissue was significantly increased and the size or fluorescence intensity of underlying tumors could be assessed more accurately. Importantly, however, lesions visible through skin flaps or after complete removal of skin were detectable in external imaging of intact mice.

Analysis of *in Vivo* GFP$^+$ Expression. s.c. plasmacytomas from GFP$^+$ cell-injected mice or s.c. tissue samples from control mice were removed immediately after sacrifice and kept in cold 1× PBS. Single-cell suspensions were prepared and analyzed by flow cytometry to compare their GFP-derived fluorescence with RPMI-8226/S-GFP$^+$ cells cultured *in vitro* as positive control *versus* non-GFP-expressing RPMI-8226/S cells as negative control. After several weeks of growth *in vivo*, RPMI-8226/S-GFP$^+$ cells explanted from s.c. plasmacytomas did not significantly differ in their GFP$^+$ expression from GFP-transfected cells cultured *in vitro* during the same period of time (Fig. 4*A*), consistent with previous reports of stable long-term fluorescence of tumor cell lines transfected with GFP vectors (5–13). Importantly, tumor cells explanted from these s.c. plasmacytomas were subsequently cultured *in vitro* for several months, confirming their viability, which is consistent with prior studies that GFP-fluorescent lesions represent viable cells (5–13) rather than accumulations of cellular debris or cells internalizing fluorescent protein from dead GFP$^+$ cells. Moreover, GFP protein irreversibly loses its fluorescence in the event of cell death (R. M. Hoffman, unpublished observations).

BM Homing of GFP$^+$ MM Cells. To confirm that GFP$^+$ MM lesions in the skeleton reflect homing of MM cells to the BM, we collected bilateral BM aspirates from femurs of mice harboring unilateral femoral GFP$^+$ lesions. BM aspirates were collected in cold PBS and directly analyzed by dual color flow cytometry, which confirmed homing to the affected femur of a distinct population of highly fluorescent cells, which was absent in the contralateral unaffected femur (Fig. 4*B*). Additional flow cytometric analyses confirmed cell surface expression of human CD38, which is expressed by RPMI-8226/S cells on fluorescent cells from affected bones (Fig. 4*C*), providing additional support of specific homing of GFP$^+$ MM cells to the BM. Interestingly, flow cytometric analyses of BM aspirates from femurs with bilateral involvement of GFP$^+$ lesions demonstrated variability in the extent of BM infiltration by GFP$^+$ MM cells, reflecting the heterogeneity of BM infiltration with MM cells noted clinically (Fig. 5).

Histopathological Analysis. Standard H&E staining of sections from specimens obtained by fluorescence imaging-guided necropsy were performed to examine the potential presence of microscopic lesions that were not detectable by macroscopic fluorescence imaging and to additionally confirm that fluorescent lesions indeed correspond to GFP$^+$ MM tumor cells. No discrepancies were revealed between histopathological examination and macroscopic data obtained by fluorescence imaging; no MM lesions were detected that were not fluorescent; and conversely, no fluorescence was attributable to normal cells of the host, confirming the very high sensitivity and spec-

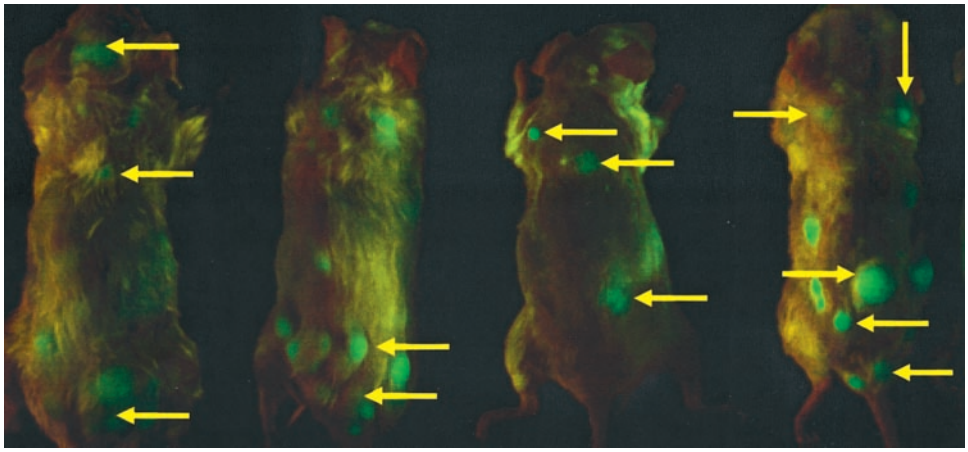

Fig. 2. Whole-body fluorescence imaging of SCID/NOD mice with diffuse GFP$^+$ MM lesions. Representative imaging results obtained from 4 mice, 4 weeks after i.v. injection of 5×10^6 RPMI-8226/S-GFP$^+$ human MM cells indicate extensive bone lesions (depicted by *yellow arrows*) in the spine, skull, lower extremities, and pelvis, as well as s.c. lesions.

Table 1 *Distribution of MM lesions in skeletal and extraskeletal sites in SCID-NOD mice injected i.v. with RPMI-8226/S-GFP$^+$ cells*

The distribution was assessed with external whole-body fluorescence imaging of mice and confirmed by fluorescence imaging-guided necropsy and conventional histopathological analyses. We detected no fluorescent lesions that did not contain MM tumor cells; conversely, no tumors were present in nonfluorescent sites, confirming the high sensitivity and specificity of fluorescence imaging-based tumor detection. The lack of overlap between the 95% CI for frequency of lesions in, *e.g.*, spine or skull *versus* other skeletal or extraskeletal lesions offers statistical confirmation ($P < 0.05$) of the nonrandom distribution of tumor lesions and their preferential involvement in the axial skeleton.

	No. of mice with GFP$^+$ lesions	(%)	95% CI
Skeletal lesions			
Overall	74	98.7	92.9–100%
Skull	64	85.3	77.3–93.3%
Parietal surface	63	84.0	75.7–92.3%
Base of skull	12	16.0	7.7–24.3%
Lower mandible	23	30.7	20.2–41.1%
Spine	72	96.0	88.9–99.7%
Cervical	12	16.0	7.7–24.3%
Thoracic	39	52.0	40.7–63.3%
Lumbar	57	76.0	66.3–85.7%
Sacral	14	18.7	9.8–27.5%
Thoracic cage	8	10.7	3.7–17.7%
Pelvis	5	6.7	1.0–12.3%
Upper extremity bones	45	60.0	48.9–71.1%
Lower extremity bones	52	69.3	58.9–79.8%
Extraskeletal lesions			
Head and neck soft tissue	2	2.7	0–6.3%
Posterior cervical soft tissue	49	65.3	54.0–75.1%
s.c. plasmacytomas	50	66.7	55.4–76.3%
Axillary region soft tissue	3	4.0	0–8.4%
Mediastinum	1	1.3	0–3.9%
Lung	1	1.3	0–3.9%
Liver	3	4.0	0–8.4%
Spleen	4	5.3	0.2–10.4%
Small and large intestine	21	28.0	17.8–38.2%
Kidneys	0	0.0	—
Paraspinal muscles	25	33.3	22.7–44.0%
Upper extremity muscles	1	1.3	0–3.9%
Lower extremity muscles	14	18.7	9.8–27.5%

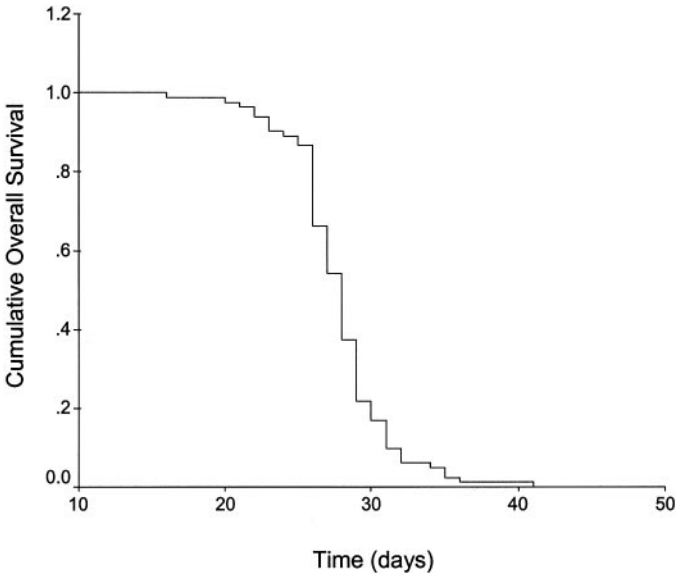

Fig. 3. Kaplan-Meier survival curve of SCID/NOD mice after i.v. injection with RPMI-8226/S-GFP$^+$ cells. Median survival of mice was 29 (95% CI: 27–30) days.

ificity of fluorescence-based detection of diffuse MM lesions. Fig. 6 depicts representative H&E staining of histological sections of bone, confirming homing of malignant plasma cells to BM at distinct skeletal sites.

Whole-Body Radiographic Analysis. Whole body radiographic analyses were performed to evaluate the presence of potential lytic lesions at the sites of fluorescent tumors. Although bone involvement in the spine was associated in some cases with radiographic lucencies analogous to lytic lesions in MM patients, radiographic analysis in this model was, in the majority of cases, not sufficiently sensitive to unequivocally detect MM lesions, suggesting that fluorescence imaging can detect tumor lesions at skeletal sites before development of lytic disease.

DISCUSSION

MM, the second most commonly diagnosed hematological malignancy in the United States, has a median overall survival of ~3 years, which has not significantly improved over the last three decades (22). Recent preclinical and early clinical studies indicate that new therapies, which target not only MM cells but also their interactions with the host BM microenvironment (14–16, 23–27), may improve out-

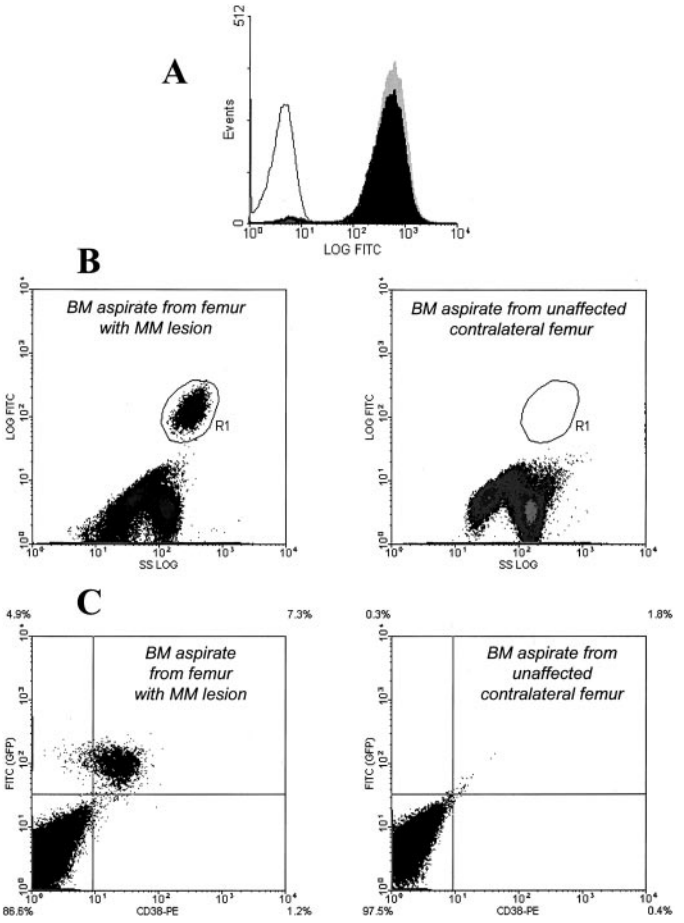

Fig. 4. *A*, representative single-color flow cytometric analysis of RPMI-8226/S-GFP$^+$ cells explanted from s.c. plasmacytomas generated after i.v. injections (■) or cultured *in vitro* (□) in G418 (500 μg/ml) selection medium for the entire duration of the *in vivo* experiment is compared with non-GFP-transfected RPMI-8226/S cells (□). After several weeks of *in vivo* growth, GFP$^+$ cells explanted from s.c. plasmacytomas maintain the same fluorescence intensity (~2 logs higher than control cells) as their counterparts cultured for the same interval *in vitro*. *B*, representative flow cytometric analyses of BM aspirates extracted from femoral bone with a GFP$^+$ lesion (*left panel*) compared with BM aspirate extracted from the contralateral femur (*right panel*), which did not harbor a GFP$^+$ lesion. In both graphs, the *x* axes represent the side scatter of cells in BM aspirate, and the *y* axes represent GFP-emitted fluorescence detected in the FL1 channel. Flow cytometry of BM aspirate from the affected femur detects a distinct population of highly fluorescent cells, included in cytometric gate R1, which is absent in the contralateral unaffected bone. *C*, representative dual color flow cytometric analysis of BM aspirates obtained from a femur with a GFP$^+$ lesion (*left panel*) *versus* its unaffected contralateral femur (*right panel*). The BM aspirate from the affected femur contains a distinct population of CD38$^+$ GFP$^+$ cells, which is absent from the unaffected contralateral bone. The detection of human CD38 on fluorescent cells of the affected bone confirms the homing to the bone of human GFP-transfected cells rather than normal cells of the host that might have incorporated fluorescent protein.

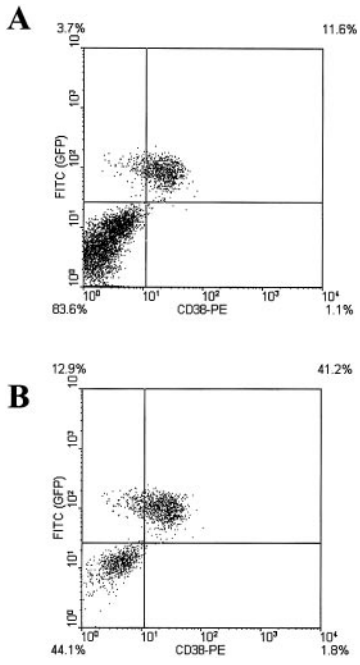

Fig. 5. Representative dual color flow cytometric analyses of BM aspirates obtained from femurs with bilateral GFP$^+$ lesions and stained with monoclonal antibody for human anti-CD38 monoclonal antibody. The analysis indicates variable extent of BM infiltration with GFP$^+$ human MM cells in the two contralateral bones, reflecting the heterogeneity of BM involvement at distinct skeletal sites in MM patients.

come of MM patients. Nonetheless, MM is still considered an invariably fatal disease, highlighting the urgent need for accelerated bench-to-bedside translation of investigational therapies. This necessitates the development of preclinical *in vivo* models that accurately simulate the clinical presentation of the disease in patients and, in particular, the homing of MM cells to the BM, a critical process in the pathophysiology of MM (28), and other hematological malignancies. Unfortunately, currently available animal models for MM are not optimal because (*a*) conventional models of s.c. implanted malignant cells are not consistent with the diffuse systemic nature of hematological malignancies and, in particular, do not reflect the close interaction of MM cells with the local BM milieu; and (*b*) diffuse tumors developing after i.v. injection cannot be readily detected and serially followed-up by conventional imaging modalities, *e.g.*, radiographic examination is often not informative of soft tissue lesions and generally is not sufficiently sensitive to monitor tumor-associated skeletal disease (29) because in rodents, which are much smaller than the human body, tumors are also much smaller and often fall below the threshold for radiographic detection (30). More sensitive imaging modalities, *e.g.*, computerized tomography or magnetic resonance imaging, currently have very high cost, which prohibits serial measurements required for large-scale screening studies of new anticancer therapies. Furthermore, the comprehensive histopathological analyses of the entire body of experimental animals might help define the distribution of tumor cells in various organs and tissues but can only be performed after necropsy and not serially during the course of administration of an antitumor regimen.

The current study fulfills the major prerequisites for a clinically relevant *in vivo* model of MM, namely the development of diffuse bone lesions, with anatomical distribution and resulting manifestations (*e.g.*, paralysis) consistent with the clinical picture of the disease in human patients and the ability to perform, with high sensitivity and specificity, noninvasive, real-time monitoring of the precise localization of tumor lesions. Indeed, MM cells, malignant counterparts of postgerminal center B-cells (28), are considered home to the BM after the venous and subsequently the arterial circulation. In that respect, our model of SCID/NOD mice injected i.v. with MM cells stably expressing GFP constitutes an orthotopic model and allows these cells to reach their preferred sites of homing, *i.e.*, the bone and form diffuse skeletal lesions, primarily in the axial skeleton, in a manner consistent with the clinical presentation of the disease. The significant visual contrast generated by the fluorescence of GFP$^+$ tumors *versus* adjacent nonfluorescent healthy tissues allows for detailed analysis by whole-body fluorescence imaging of total number and size of even small tumors, which might otherwise escape detection. The use, during necropsy of sacrificed mice, of fluorescence imaging-guided sampling of tissue specimens with fluorescent lesions, and subsequent histopathological analyses confirmed, in this study, the very high sensitivity and specificity of whole-body fluorescent imaging in this GFP$^+$ model. The selective noninvasive macroscopic visualization of tumor burden without exogenous use of contrast agents, radioactivity, fluorescent antibodies, or other preparative procedures that might limit the application of this model or confound interpretation of its results (13), allows for minimal alterations in tumor cell behavior *in vivo* (31). Furthermore, collection of whole-body fluorescence imaging data does not require (in contrast to other imaging modalities) lengthy exposures of immobilized animals and was performed with only short-acting anesthetics (*e.g.*, isofluorane), which did not adversely impact on the survival of mice, in this study.

Our study also indicates that in mice with diffuse MM lesions, the

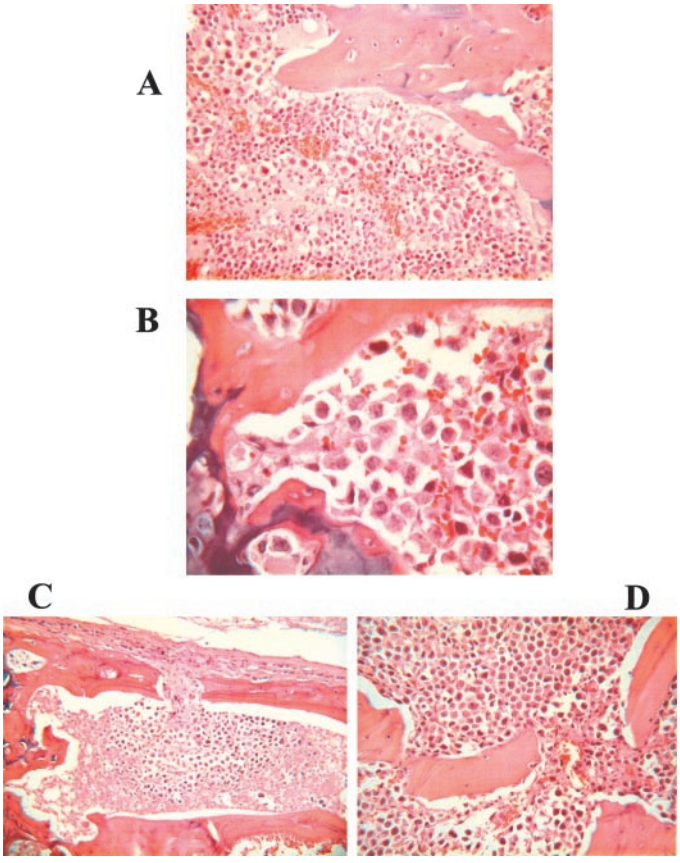

Fig. 6. Representative histopathological analyses (H&E staining) of BM sections at sites of GFP$^+$ MM lesions. All panels are characterized by extensive BM infiltration by malignant plasma cells (*A–D*), and variable degrees of infiltration in cortical bone. *A* (×50 magnification) and *B* (×100 magnification) depict pronounced infiltration of the BM in the distal epiphysis of the femur. *C*, the almost complete infiltration of the BM cavity of a lumbar spine vertebral body (×20). *D*, invasion of RPMI-8226/S-GFP$^+$ cells through bone structures (×50).

overall survival and quality of life are not affected by the total tumor burden in a strictly proportional manner. Indeed, vertebral bone lesions (which can be of a relatively small size in comparison to the overall tumor burden) were the cause of paralysis and sacrifice in the overwhelming majority of mice, whereas lesions in other less critical skeletal or extraskeletal (*e.g.,* s.c. tissues) areas with greater local tumor involvement did not have the same impact on the course of the disease. These findings suggest that systemic markers of total tumor burden (*e.g.,* serum or urine levels of monoclonal immunoglobulins in MM or other plasma cell dyscrasias), although informative of its overall changes during the course of the disease, may not reflect how individual tumor lesions at various organs can differentially affect the survival and quality of life of mice. Importantly, the critical role of the local bone microenvironment in conferring drug resistance not only to MM cell but also to cells from other osteotropic malignancies (3, 32) indicates that systemic markers of total tumor burden may not reliably reflect how tumor cells homing in different organs may differentially respond to therapy because of differential interactions within the distinct local microenvironments of the various host tissues.

Because of these differential, site-dependent interactions of tumor cells with the local microenvironment, it is important for *in vivo* animal models of systemic malignancies such as MM to mimic the patterns of organ involvement, clinical course, and manifestations of the disease in patients. In this study, the SCID/NOD model of diffuse GFP^+ MM lesions simulated the clinical behavior of MM more closely than conventional models of ectopic s.c. implantation of human MM cells (6) because >95% of mice injected with GFP^+ MM cells developed bone lesions at one or more sites in the spine, and at least one tumor site in the axial skeleton was noted in 98% of SCID/NOD mice, which mirrors the osteotropic behavior of MM in patients (30). Importantly, GFP^+ MM lesions targeted mainly the axial skeleton, which is consistent with the actual pattern of anatomical distribution of MM bone disease observed clinically (30). The clinical relevance of this model is additionally highlighted by the high incidence of clinical manifestations directly attributed to bone lesions, including the development of paralysis secondary to vertebral MM involvement.

Because of its clinical relevance, this GFP^+ MM mouse model provides a valuable experimental setting to preclinically evaluate the *in vivo* antitumor activity of investigational agents. Indeed, recent studies of our group have applied this model not only to evaluate the antimyeloma activity of new therapeutic approaches such as the heat shock protein 90 inhibitors (33) but also to elucidate the *in vivo* molecular sequelae of such therapies and confirm that they are consistent with their *in vivo* mechanism(s) of action. This is possible because GFP^+ MM cells can be purified on the basis of their fluorescence using flow cytometry-based cell sorting from nonfluorescent normal host cells and subsequently analyzed by conventional or high-throughput molecular studies of gene expression or proteomic profile (33). Of note, in ongoing studies from our group using other GFP-expressing human MM cell lines (*e.g.,* MM-1S, MM-1R, OPM-1) we have also found formation of MM bone lesions in SCID/NOD mice, similarly to the current results with RPMI-8226/S-GFP cells.[5] Although the precise anatomical pattern of lesions generated by each line can depend on its individual molecular characteristics (and can potentially differ among different sublines or subclones of the same line if these exhibit different osteotropic potential), the tendency of MM cells for establishment of bone lesions is not limited to RPMI-8226-derived cells. Furthermore, these findings indicate that fluorescence imaging of diffuse MM bone lesions is applicable for a broader spectrum of MM cell lines. In addition, whole-body fluorescence imaging for detection of MM cells can also be incorporated in the setting of other of other *in vivo* MM models such as syngeneic mouse models of MM (*e.g.,* by GFP-expressing 5T2 mouse MM cells injected in C57BL/KaLwRij mice; Ref. 34, 35), as well as in the SCID-hu model of MM (36, 37). In this latter model, direct injection of human MM cells in human bone grafts implanted in SCID mice leads to osteolytic lesions in the injected graft, as well as to a secondary (metastatic) bone lesion in contralateral human bone grafts not injected with MM cells. These models, which have provided important insight in the pathophysiology of the osteolytic lesions of MM, may be complemented by injection of GFP^+ human MM cells to allow for better monitoring of the MM tumor burden (and its response to therapy) in the bone grafts and to facilitate the characterization of interactions between MM cells and the BM microenvironment.

Furthermore, because of its clinical relevance, this *in vivo* model is not only appropriate for preclinical evaluation of potential new therapies but also for addressing important questions regarding the pathophysiology of MM. Of particular biological significance is the marked osteotropism of MM cells and their heterogeneous but not random skeletal distribution. The degree of BM infiltration by GFP^+ MM cells, as assessed by flow cytometry of BM aspirates, was not uniform but heterogeneous and analogous to the variable percentage of BM infiltration by malignant plasma cells in different skeletal sites in the same patients noted clinically. Furthermore, detailed statistical analyses, including calculation of 95% CIs for the frequencies of tumor involvement in individual organ sites confirmed that the distribution of tumor lesions was not random and involved preferential bone involvement in the bones and, primarily, in the axial skeleton, which is characterized by the presence of trabecular bone, a major site of MM bone involvement in human patients. The precise etiology for this site-specific pattern of tumor formation is under investigation using this GFP^+ MM model. It conceivable that the mechanism underlying this site specificity is multifactorial and could include heterogeneous expression of cytokines, growth factors, and/or adhesion molecules in different parts of the skeleton. Because MM cell proliferation and survival is significantly enhanced by BM-derived cytokines such as insulin-like growth factors (38) and interleukin 6 (32) or by binding of MM cells to the ECM or stromal cells in the BM (2), it is possible that skeletal areas with most frequent establishment of MM lesions represent areas with, *e.g.,* higher local production of proliferative/antiapoptotic factors for MM cells, enhanced activity of BMSCs, and/or expression of specific ECM components. Interestingly, axial skeletal areas most frequently targeted by MM lesions also harbor active red BM (39), a principal site for adult hematopoiesis: the very active local network of BMSCs in those sites may not offer support via cytokine- or cell adhesion-mediated pathways not only for normal hematopoietic lineages but also for locally seeded tumor cells. The nonrandom distribution of MM lesions could also be due, at least in part, to well-documented organ- or tissue-specific molecular heterogeneity of the vascular tree (40, 41). Indeed, *in vivo* screening of phage-displayed peptide libraries has identified peptide sequences capable of homing selectively to the vasculature of specific organs (42). Such organ- or tissue-specific vascular markers may not only facilitate organ-specific blood-tissue exchange of biomolecules or selective homing of normal cells, *e.g.,* migration of neutrophils to inflamed tissues, lymphocyte homing to lymphoid tissues (43–45), but may also function as receptors for metastasizing malignant cells (46–48), thus determining, *e.g.,* the osteotropism of MM cells. Our study's finding of more frequent bone lesions in the axial skeleton raise the hypothesis that the concept of heterogeneous molecular signature of the vasculature may apply not only to different tissues but

[5] C. S. Mitsiades *et al.*, unpublished observation.

maybe to different parts of the same organ or tissue, *e.g.*, in axial skeleton *versus* other bone regions. Determination of such axial skeleton-specific endothelial markers could serve to design new therapeutic strategies specifically delivering antitumor agents in sites of predominant MM cell homing as in previous studies of selective vascular targeting of metastatic disease (49, 50).

Although GFP^+ MM cells predominantly homed to the bones, extraskeletal tumors were also observed in our model. Some of these plasmacytomas, *e.g.*, paraspinal soft tissue GFP^+ lesions, resulted from direct extension of plasma cell infiltration from adjacent bone lesions. Other extraskeletal tumors such as s.c. plasmacytomas may reflect the derivation of RPMI-8226/S cells from circulating malignant plasma cells of a patient with advanced MM (plasma cell leukemia; Ref. 51). At this stage of the disease, MM cells have acquired additional genetic abnormalities, allowing them to survive in the absence of interaction with the BM microenvironment. Importantly, however, the striking osteotropic behavior of these cells, with bone involvement in almost all mice of our study, indicates that the BM milieu can still play an important role in promoting the proliferation and survival of even very aggressive MM cells.

This study, which represents a first application of whole-body fluorescence imaging *in vivo* models for the study of MM may also be applied to evaluate the development of diffuse lesions in other hematological malignancies, provides the context for additional characterization of disease pathogenesis and, importantly, establishes a clinically relevant framework for preclinical testing of new therapeutic strategies.

REFERENCES

1. Kuehl, W. M., and Bergsagel, P. L. Multiple myeloma: evolving genetic events and host interactions. Nat. Rev. Cancer, *2:* 175–187, 2002.
2. Damiano, J. S., Cress, A. E., Hazlehurst, L. A., Shtil, A. A., and Dalton, W. S. Cell adhesion mediated drug resistance (CAM-DR): role of integrins and resistance to apoptosis in human myeloma cell lines. Blood, *93:* 1658–1667, 1999.
3. Mitsiades, C. S., and Koutsilieris, M. Molecular biology and cellular physiology of refractoriness to androgen ablation therapy in advanced prostate cancer. Expert Opin. Investig. Drugs, *10:* 1099–1115, 2001.
4. Pilarski, L. M., Hipperson, G., Seeberger, K., Pruski, E., Coupland, R. W., and Belch, A. R. Myeloma progenitors in the blood of patients with aggressive or minimal disease: engraftment and self-renewal of primary human myeloma in the bone marrow of NOD SCID mice. Blood, *95:* 1056–1065, 2000.
5. Yang, M., Baranov, E., Wang, J. W., Jiang, P., Wang, X., Sun, F. X., Bouvet, M., Moossa, A. R., Penman, S., and Hoffman, R. M. Direct external imaging of nascent cancer, tumor progression, angiogenesis, and metastasis on internal organs in the fluorescent orthotopic model. Proc. Natl. Acad. Sci. USA, *99:* 3824–3829, 2002.
6. Yang, M., Baranov, E., Li, X. M., Wang, J. W., Jiang, P., Li, L., Moossa, A. R., Penman, S., and Hoffman, R. M. Whole-body and intravital optical imaging of angiogenesis in orthotopically implanted tumors. Proc. Natl. Acad. Sci. USA, *98:* 2616–2621, 2001.
7. Bouvet, M., Wang, J., Nardin, S. R., Nassirpour, R., Yang, M., Baranov, E., Jiang, P., Moossa, A. R., and Hoffman, R. M. Real-time optical imaging of primary tumor growth and multiple metastatic events in a pancreatic cancer orthotopic model. Cancer Res., *62:* 1534–1540, 2002.
8. Yang, M., Baranov, E., Jiang, P., Sun, F. X., Li, X. M., Li, L., Hasegawa, S., Bouvet, M., Al-Tuwaijri, M., Chishima, T., Shimada, H., Moossa, A. R., Penman, S., and Hoffman, R. M. Whole-body optical imaging of green fluorescent protein-expressing tumors and metastases. Proc. Natl. Acad. Sci. USA, *97:* 1206–1211, 2000.
9. Yang, M., Jiang, P., Sun, F. X., Hasegawa, S., Baranov, E., Chishima, T., Shimada, H., Moossa, A. R., and Hoffman, R. M. A fluorescent orthotopic bone metastasis model of human prostate cancer. Cancer Res., *59:* 781–786, 1999.
10. Yang, M., Hasegawa, S., Jiang, P., Wang, X., Tan, Y., Chishima, T., Shimada, H., Moossa, A. R., and Hoffman, R. M. Widespread skeletal metastatic potential of human lung cancer revealed by green fluorescent protein expression. Cancer Res., *58:* 4217–4221, 1998.
11. Hoffman, R. M. Orthotopic transplant mouse models with green fluorescent protein-expressing cancer cells to visualize metastasis and angiogenesis. Cancer Metastasis Rev., *17:* 271–277, 1998.
12. Chishima, T., Yang, M., Miyagi, Y., Li, L., Tan, Y., Baranov, E., Shimada, H., Moossa, A. R., Penman, S., and Hoffman, R. M. Governing step of metastasis visualized *in vitro*. Proc. Natl. Acad. Sci. USA, *94:* 11573–11576, 1997.
13. Chishima, T., Miyagi, Y., Wang, X., Yamaoka, H., Shimada, H., Moossa, A. R., and Hoffman, R. M. Cancer invasion and micrometastasis visualized in live tissue by green fluorescent protein expression. Cancer Res., *57:* 2042–2047, 1997.
14. Mitsiades, C. S., Treon, S. P., Mitsiades, N., Shima, Y., Richardson, P., Schlossman, R., Hideshima, T., and Anderson, K. C. TRAIL/Apo2L ligand selectively induces apoptosis and overcomes drug resistance in multiple myeloma: therapeutic applications. Blood, *98:* 795–804, 2001.
15. Mitsiades, N., Mitsiades, C. S., Poulaki, V., Chauhan, D., Richardson, P. G., Hideshima, T., Munshi, N., Treon, S. P., and Anderson, K. C. Biologic sequelae of nuclear factor-κB blockade in multiple myeloma: therapeutic applications. Blood, *99:* 4079–4086, 2002.
16. Mitsiades, N., Mitsiades, C. S., Poulaki, V., Anderson, K. C., and Treon, S. P. Intracellular regulation of tumor necrosis factor-related apoptosis-inducing ligand-induced apoptosis in human multiple myeloma cells. Blood, *99:* 2162–2171, 2002.
17. Kaplan, E., and Meier, P. Non-parametric estimation for incomplete observations. J. Am. Stat. Assoc., *53:* 457–481, 1958.
18. Spilker, B. Guide to Clinical Trials, p. xxv, 1156. New York: Raven Press, 1991.
19. Sasaki, A., Boyce, B. F., Story, B., Wright, K. R., Chapman, M., Boyce, R., Mundy, G. R., and Yoneda, T. Bisphosphonate risedronate reduces metastatic human breast cancer burden in bone in nude mice. Cancer Res., *55:* 3551–3557, 1995.
20. Hughes, D. E., Dai, A., Tiffee, J. C., Li, H. H., Mundy, G. R., and Boyce, B. F. Estrogen promotes apoptosis of murine osteoclasts mediated by TGF-β. Nat. Med., *2:* 1132–1136, 1996.
21. Guise, T. A., Yin, J. J., Taylor, S. D., Kumagai, Y., Dallas, M., Boyce, B. F., Yoneda, T., and Mundy, G. R. Evidence for a causal role of parathyroid hormone-related protein in the pathogenesis of human breast cancer-mediated osteolysis. J. Clin. Investig., *98:* 1544–1549, 1996.
22. Bataille, R., and Harousseau, J. L. Multiple myeloma. N. Engl. J. Med., *336:* 1657–1664, 1997.
23. Hideshima, T., Chauhan, D., Richardson, P., Mitsiades, C., Mitsiades, N., Hayashi, T., Munshi, N., Dang, L., Castro, A., Palombella, V., Adams, J., and Anderson, K. C. NF-κB as a therapeutic target in multiple myeloma. J. Biol. Chem., *277:* 16639–16647, 2002.
24. Mitsiades, N., Mitsiades, C. S., Poulaki, V., Chauhan, D., Richardson, P. G., Hideshima, T., Munshi, N. C., Treon, S. P., and Anderson, K. C. Apoptotic signaling induced by immunomodulatory thalidomide analogs in human multiple myeloma cells: therapeutic implications. Blood, *99:* 4525–4530, 2002.
25. Hideshima, T., Richardson, P., Chauhan, D., Palombella, V. J., Elliott, P. J., Adams, J., and Anderson, K. C. The proteasome inhibitor PS-341 inhibits growth, induces apoptosis, and overcomes drug resistance in human multiple myeloma cells. Cancer Res., *61:* 3071–3076, 2001.
26. Hideshima, T., Chauhan, D., Shima, Y., Raje, N., Davies, F. E., Tai, Y. T., Treon, S. P., Lin, B., Schlossman, R. L., Richardson, P., Muller, G., Stirling, D. I., and Anderson, K. C. Thalidomide and its analogs overcome drug resistance of human multiple myeloma cells to conventional therapy. Blood, *96:* 2943–2950, 2000.
27. Mitsiades, N., Mitsiades, C. S., Poulaki, P., Chauhan, D., Gu, X., Bailey, C., Joseph, M., Libermann, T. A., Treon, S. P., Munshi, N. C., Richardson, P. G., Hideshima, T., and Anderson, K. C. Molecular sequelae of proteasome inhibition in human multiple myeloma cells. Proc. Natl. Acad. Sci. USA, *99:* 14374–14379, 2002.
28. Hallek, M., Bergsagel, P. L., and Anderson, K. C. Multiple myeloma: increasing evidence for a multistep transformation process. Blood, *91:* 3–21, 1998.
29. Hjorth-Hansen, H., Seifert, M. F., Borset, M., Aarset, H., Ostlie, A., Sundan, A., and Waage, A. Marked osteoblastopenia and reduced bone formation in a model of multiple myeloma bone disease in severe combined immunodeficiency mice. J. Bone Miner Res., *14:* 256–263, 1999.
30. Healy, J. C., and Armstrong, P. Radiological features of multiple myeloma. *In:* J. S. Malpas, D. E. Bergsagel, R. A. Kyle, and K. C. Anderson (eds.), Myeloma, Biology and Management, Ed. 2, pp. 233–265. New York: Oxford University Press, 1998.
31. Zhao, M., Yang, M., Baranov, E., Wang, X., Penman, S., Moossa, A. R., and Hoffman, R. M. Spatial-temporal imaging of bacterial infection and antibiotic response in intact animals. Proc. Natl. Acad. Sci. USA, *98:* 9814–9818, 2001.
32. Anderson, K. Advances in the biology of multiple myeloma: therapeutic applications. Semin. Oncol., *26:* 10–22, 1999.
33. Mitsiades, C. S., Mitsiades, N., Poulaki, V., Fanourakis, G., Hideshima, T., Chauhan, D., Munshi, N. C., and Anderson, K. C. Hsp90 inhibitors prolong survival in a SCID/NOD mice model of diffuse multiple myeloma: therapeutic implications. Blood, *100:* 106a, 2002.
34. Radl, J., De Glopper, E. D., Schuit, H. R., and Zurcher, C. Idiopathic paraproteinemia. II. Transplantation of the paraprotein-producing clone from old to young C57BL/KaLwRij mice. J. Immunol., *122:* 609–613, 1979.
35. Croese, J. W., Vas Nunes, C. M., Radl, J., van den Enden-Vieveen, M. H., Brondijk, R. J., and Boersma, W. J. The 5T2 mouse multiple myeloma model: characterization of 5T2 cells within the bone marrow. Br. J. Cancer, *56:* 555–560, 1987.
36. Urashima, M., Chen, B. P., Chen, S., Pinkus, G. S., Bronson, R. T., Dedera, D. A., Hoshi, Y., Teoh, G., Ogata, A., Treon, S. P., Chauhan, D., and Anderson, K. C. The development of a model for the homing of multiple myeloma cells to human bone marrow. Blood, *90:* 754–765, 1997.
37. Yaccoby, S., Barlogie, B., and Epstein, J. Primary myeloma cells growing in SCID-hu mice: a model for studying the biology and treatment of myeloma and its manifestations. Blood, *92:* 2908–2913, 1998.
38. Mitsiades, C. S., Mitsiades, N., Poulaki, V., Schlossman, R., Akiyama, M., Chauhan, D., Hideshima, T., Treon, S. P., Munshi, N. C., Richardson, P. G., and Anderson, K. C. Activation of NF-κB and up-regulation of intracellular anti-apoptotic proteins via the IGF-1/Akt signaling in human multiple myeloma cells: therapeutic implications. Oncogene, *21:* 5673–5683, 2002.
39. Steiner, R. M., Mitchell, D. G., Rao, V. M., Murphy, S., Rifkin, M. D., Burk, D. L., Jr., Ballas, S. K., and Vinitski, S. Magnetic resonance imaging of bone marrow: diagnostic value in diffuse hematologic disorders. Magn. Reson. Q, *6:* 17–34, 1990.

40. Augustin, H. G., Kozian, D. H., and Johnson, R. C. Differentiation of endothelial cells: analysis of the constitutive and activated endothelial cell phenotypes. Bioessays, *16:* 901–906, 1994.
41. Rajotte, D., Arap, W., Hagedorn, M., Koivunen, E., Pasqualini, R., and Ruoslahti, E. Molecular heterogeneity of the vascular endothelium revealed by *in vivo* phage display. J. Clin. Investig., *102:* 430–437, 1998.
42. Pasqualini, R., and Ruoslahti, E. Organ targeting *in vivo* using phage display peptide libraries. Nature (Lond.), *380:* 364–366, 1996.
43. Salmi, M., and Jalkanen, S. How do lymphocytes know where to go: current concepts and enigmas of lymphocyte homing. Adv. Immunol., *64:* 139–218, 1997.
44. Streeter, P. R., Berg, E. L., Rouse, B. T., Bargatze, R. F., and Butcher, E. C. A tissue-specific endothelial cell molecule involved in lymphocyte homing. Nature (Lond.), *331:* 41–46, 1988.
45. Berg, E. L., Goldstein, L. A., Jutila, M. A., Nakache, M., Picker, L. J., Streeter, P. R., Wu, N. W., Zhou, D., and Butcher, E. C. Homing receptors and vascular addressins: cell adhesion molecules that direct lymphocyte traffic. Immunol. Rev., *108:* 5–18, 1989.
46. Auerbach, R., Lu, W. C., Pardon, E., Gumkowski, F., Kaminska, G., and Kaminski, M. Specificity of adhesion between murine tumor cells and capillary endothelium: an *in vitro* correlate of preferential metastasis *in vivo*. Cancer Res., *47:* 1492–1496, 1987.
47. Pauli, B. U., Augustin-Voss, H. G., el-Sabban, M. E., Johnson, R. C., and Hammer, D. A. Organ-preference of metastasis. The role of endothelial cell adhesion molecules. Cancer Metastasis Rev., *9:* 175–189, 1990.
48. Johnson, R. C., Augustin-Voss, H. G., Zhu, D. Z., and Pauli, B. U. Endothelial cell membrane vesicles in the study of organ preference of metastasis. Cancer Res., *51:* 394–399, 1991.
49. Arap, W., Pasqualini, R., and Ruoslahti, E. Cancer treatment by targeted drug delivery to tumor vasculature in a mouse model. Science (Wash. DC), *279:* 377–380, 1998.
50. Ruoslahti, E., and Rajotte, D. An address system in the vasculature of normal tissues and tumors. Annu. Rev. Immunol., *18:* 813–827, 2000.
51. Matsuoka, Y., Moore, G. E., Yagi, Y., and Pressman, D. Production of free light chains of immunoglobulin by a hematopoietic cell line derived from a patient with multiple myeloma. Proc. Soc. Exp. Biol. Med., *125:* 1246–1250, 1967.